

Supplementary Materials

New Ground-State Crystal Structure of Elemental Boron

Qi An,¹⁺ K. Madhav Reddy,²⁺ Kelvin. Y. Xie², Kevin J. Hemker,^{2*} and William A. Goddard III^{1*}

¹*Materials and Process Simulation Center, California Institute of Technology, Pasadena, CA 91125, U. S. A.*

²*Department of Mechanical Engineering, Johns Hopkins University, Baltimore, MD 21210, USA*

⁺ These authors contributed equally to this work

*Corresponding author E-mail: hemker@jhu.edu, wag@wag.caltech.edu,

Methods

1. Computational details

All simulations were performed using the Vienna Ab-initio Simulation Package (VASP) periodic code with plane wave basis sets [32–34]. We used an energy cutoff of 600 eV in all the simulations since it gives excellent convergence on energy, force, stress, and geometries. The energy error for terminating electronic self-consistent field (SCF) and the force criterion for the geometry optimization were set equal to 10^{-6} eV and 10^{-3} eV/Å, respectively.

Reciprocal space was sampled using the Γ -centered Monkhorst–Pack scheme with a fine resolution of $2\pi \times 1/40$ Å⁻¹ for all boron polymorphs.

We used the projector-augmented wave pseudopotentials for the Perdew–Burke–Ernzerhof (PBE) exchange-correlation functional [35].

We performed the natural bond orbital (NBO) analysis [46] to calculate the charges of each atom and the charges were accumulated in B₁₂ and B₅₇ units to obtain the charges distributions in β and τ phases.

All the calculated structures are in separated cif files including in SM.

2. Material characterization

The commercial β -boron powders used in this study were procured from H. C. Starck. The grain size ranged from few hundred nanometers (nm) to several micrometers (μm) in size. The powders were characterized using Cu-K α radiation at a wavelength of 1.54 Å by X-ray diffraction (XRD) using Bruker D8 Advance system (Bruker AXS GmbH, Germany), operated at 30 kV and 40 mA. XRD data were collected at a step size and step time of 0.02 degree and 5 second for 2-theta. Specimens for TEM were prepared by powder dispersion on holey carbon film coated Cu grids. HRTEM imaging was carried out at 300 keV, while selected area electron diffraction (SAED) was used to study the crystallographic information, using a Philips FEI CM-300 FEG. Electron energy loss spectroscopy (EELS) was performed with a Gatan detector on the CM-300 FEG and used to determine the local composition of the powder particles. HRTEM phase contrast image simulations were performed using xHREM software (HREM Research Inc.) and a multislice routine that used the QM structure model as an input file. The imaging conditions used in simulation and experiments were as follows: the incident electron beam energy was 300 keV, the spherical aberration coefficient (Cs) was 1.2 mm, the energy spread was 10 nm, the beam convergence was 0.3 and 0.4 nm⁻¹, the defocus and thickness were varied from + (20-50) nm and 2 to 50 nm.

3. HRTEM image simulation

The previously reported β -B [37, 38] and new QM predicted τ -B structures were used as input files for the xHREM program. As shown in Fig S1 (b, c), simulated HRTEM images calculated using the β -B input file and the following parameters (spherical aberration coefficient $C_3 = 1.2$ mm, beam convergence = 0.04 \AA^{-1} , aperture radius = 100 \AA^{-1} , defocus spread = 100 \AA , specimen thickness = 400 \AA and defocus were = -2500 \AA) were found to match the experimentally acquired HRTEM images that were obtained at 300 KeV using a Philips FEI CM-300 FEG. As shown in Fig. 3 (b, c), simulated HRTEM images calculated using the τ -B structure and the following input parameters (spherical aberration coefficient $C_3=1.2$ mm, beam convergence = 0.03 \AA^{-1} , aperture radius = 100 \AA^{-1} , defocus spread = 100 \AA , specimen thickness = 60 \AA and defocus were = $+200 \text{ \AA}$) were found to match the remaining experimental HRTEM images.

4. Selected area electron diffraction simulation

Diffraction simulations were carried out using Crystal Maker® software and input files for the atomic positions for both the previously reported β -B [39, 40] structure and the newly observed and QM predicted τ -B. Direct comparisons between the experimental and simulated SAED patterns (e.g. Fig 3(d) and (e); and Fig S1 (d) and (e)) allowed us to identify both the structure and the orientation of individual grains.

Table S1. The predicted absolute energies (eV/atom) and cohesive energy of various boron phases from VASP. Dispersion correction and zero point energy are included in the absolute energy.

Structure	α -B ₁₂	β -B ₁₀₅	β -B ₁₀₆	τ -B ₁₀₅	τ -B ₁₀₆	γ -B ₂₈	B-atom
Energy (eV/atom)	-6.6791	-6.6538	-6.6780	-6.6794	-6.6918	-6.6519	-0.2879
Include dispersion	-6.7832	-6.7506	-6.7755	-	-6.7893	-6.7600	-
Include ZPE and dispersion	-6.6532	-	-6.6489	-	-6.6627	-	-
Cohesive energy	6.3912	6.3659	6.3901	6.3915	6.4039	6.3640	-

Figure S1

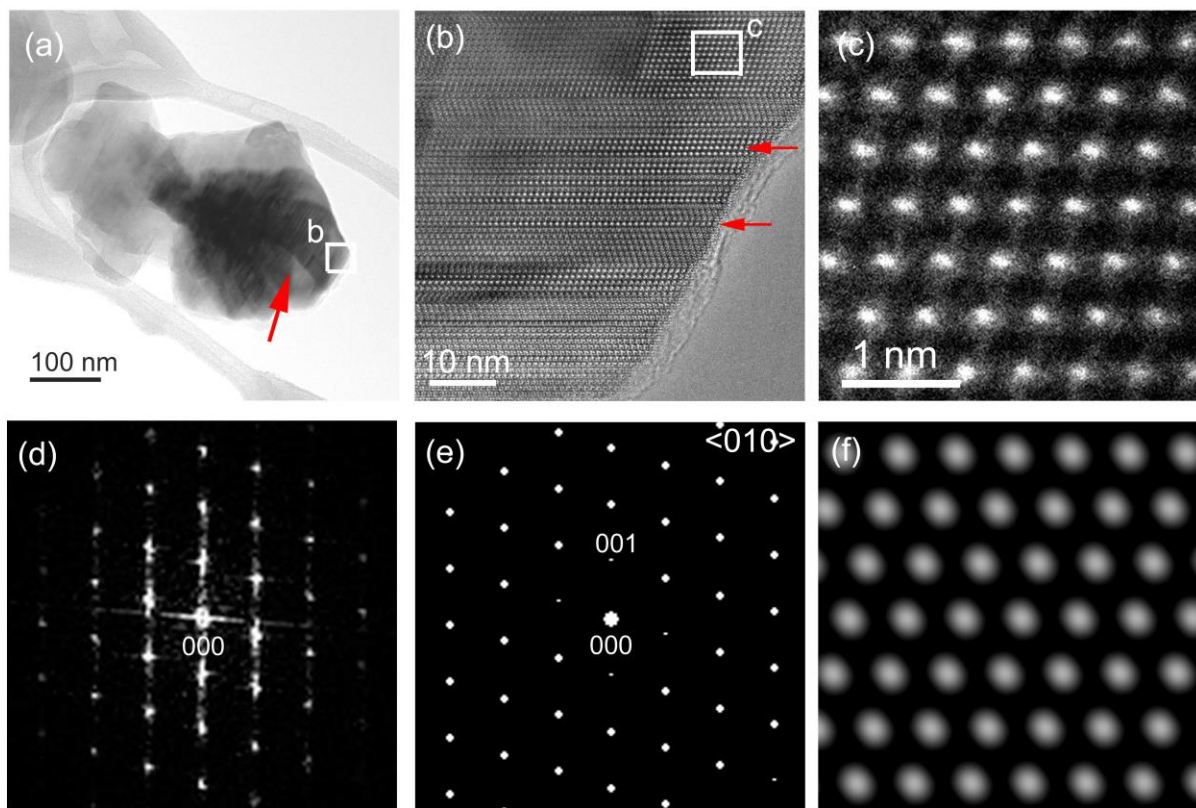


Figure S1. TEM characterization of β -B. (a) A typical low magnification TEM image showing the powder morphology. (b) Higher magnification phase contrast image of the thin region of the boron structure viewed along the $\langle 010 \rangle$ zone axis. The planar faults (*i.e.*, twins and stack faults) within the grains are marked with red arrows and are similarly to those previously observed in β -B [41, 42]. (c) Experimental HRTEM image displaying the ordered rhombohedral structure of β -B. (d) An experimental fast Fourier transform (FFT) pattern taken from the region imaged in (c) that indexes to be the β -B structure. (e) A calculated SAED pattern from the structure model of β -B, projected along the $\langle 010 \rangle$ orientation, matches well with experimental pattern. In the experimental and simulated pattern (000) represents the transmitted beam. (f) A simulated HRTEM image calculated using the β -B structure consists of 105 atoms unit cell that matches the experimental image.

Figure S2

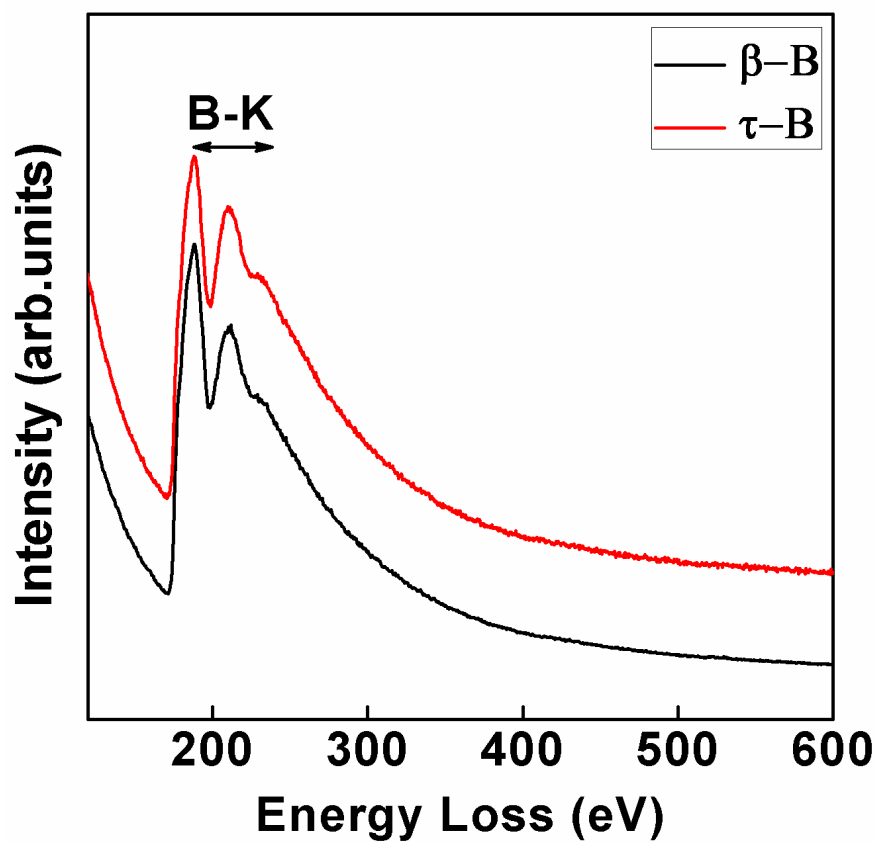


Figure S2. A representative high-energy loss spectrum from both the β -boron and τ -boron particles showing that the only prominent EELS signal is the (B-K) edge, thus confirming that the individual grains are pure boron.

Figure S3

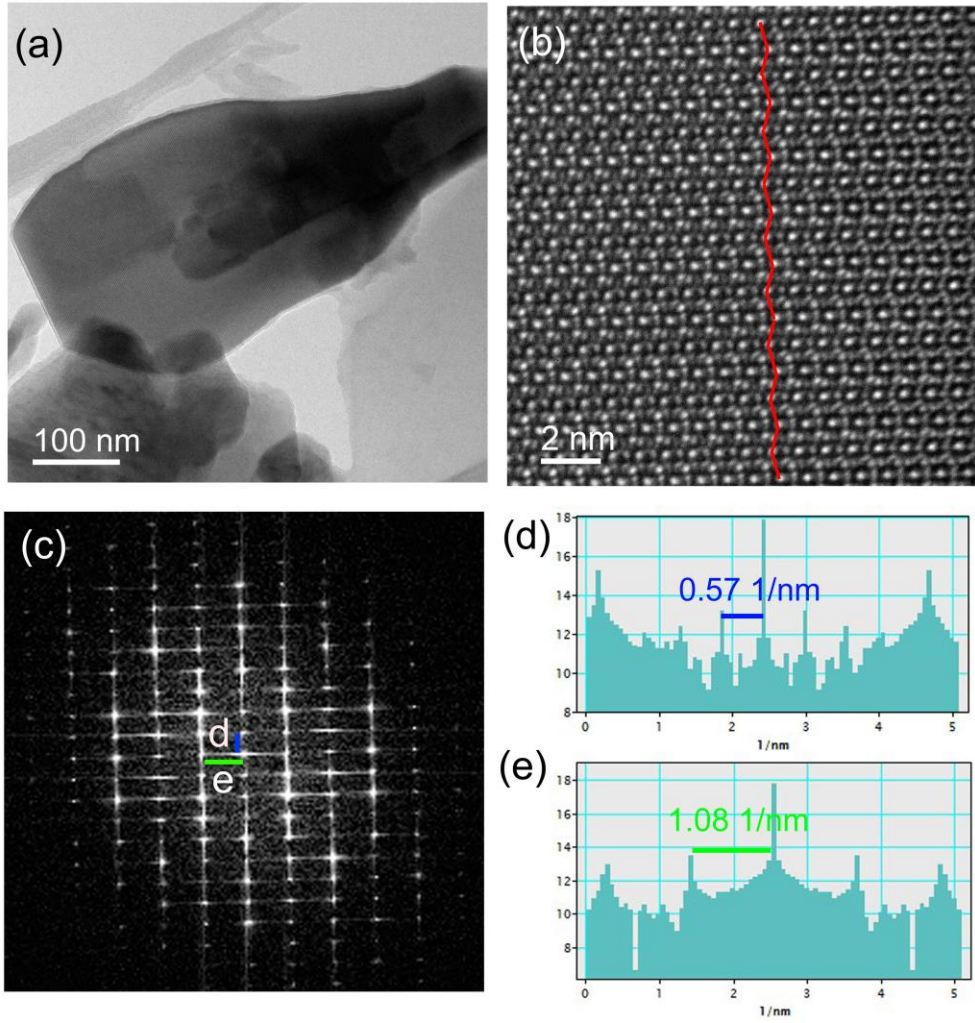


Figure S3. TEM characterization of the newly observed τ -B phase along a $\langle 010 \rangle$ zone axis. (a) A representative low magnification TEM image shows the plate-like morphology with no apparent diffraction contrast of conventional twins and stack faults when oriented along the $\langle 010 \rangle$ zone axis. (b) HRTEM images show kinks at every other layer. (c) FFT pattern taken from the same region as (b) showing that the grain is parallel to the $\langle 010 \rangle$ orientation. (d) The measured lattice spacing from the reciprocal Fourier transform in vertical (d) and horizontal (e) directions from the direct beam (000) suggests a lattice spacing ratio of approximately 1:1.9 ratio that matches closely with QM calculated ratio of 1:1.9 as explained in the manuscript.

Figure S4

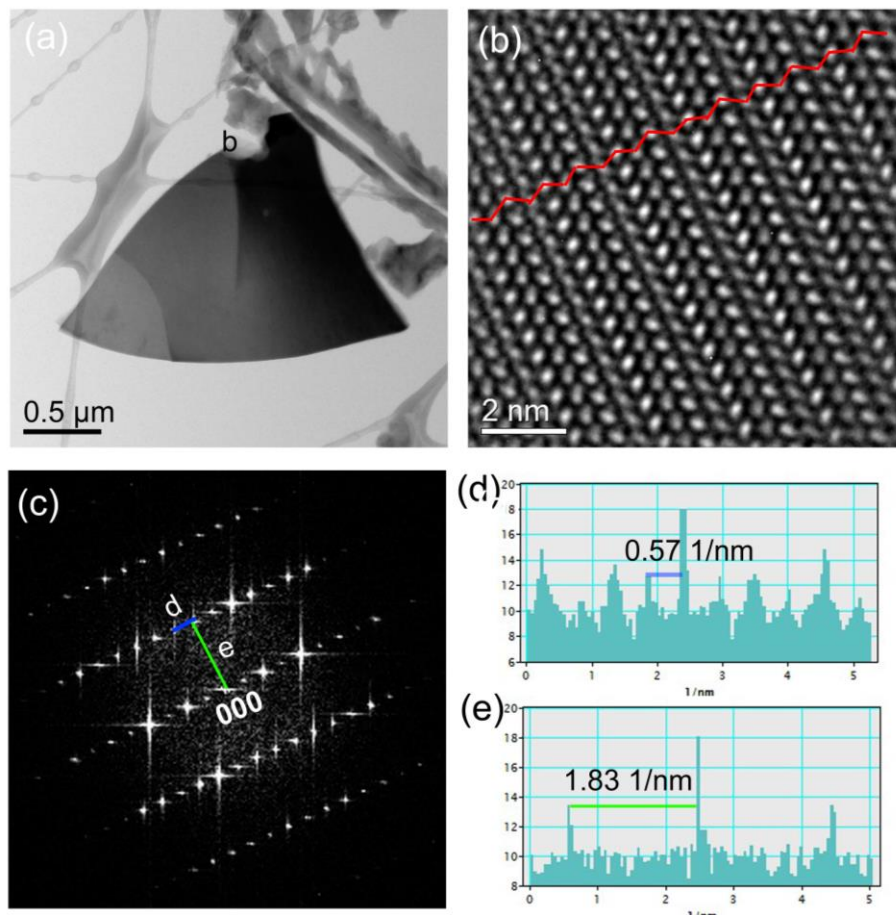


Figure S4. TEM characterization of newly observed τ -B phase along a $\langle 110 \rangle$ zone axis. (a) A typical low magnification TEM image shows the plate-like morphology. (b) HRTEM images shows kinks highlighted with red lines. (c) FFT pattern taken from the same region of (b) showing evidence of the grain aligned along a $\langle 110 \rangle$ orientation. (d) The measured lattice spacing from the reciprocal Fourier transform in parallel (d) and perpendicular (e) from (000) is $\sim 1:3.2$

Figure S5

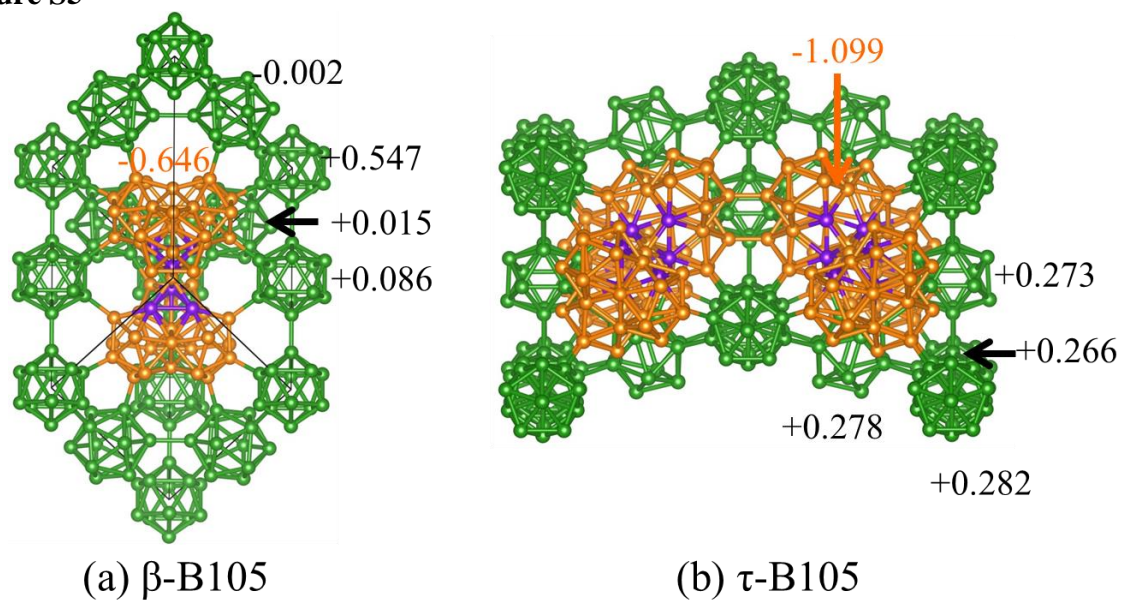


Figure S5. Charge distributions (NBO analysis) of B_{12} and B_{57} units in β -B105 and τ -B105 structures. The τ -B₁₀₅ structure makes more charge transfer from B_{57} units to B_{12} units, leading to more stable B_{12} and B_{57} units. The B_{12} and the B_{28} units are represented by green and orange balls, respectively, except that the B_{13} sites are represented by purple balls.

References

- [32] G. Kresse and J. Hafner, *Phys. Rev. B* **47**, 558 (1993).
- [33] G. Kresse and J. Furthmuller, *Comput. Mater. Sci.* **6**, 15 (1996).
- [34] G. Kresse and J. Furthmüller, *Phys. Rev. B* **16**, 11169 (1996).
- [35] G. Kresse and D. Joubert, *Phys. Rev. B* **59**, 1758 (1999).
- [36] B. D. Dunnington and J. R. Schmidt, *J. Chem. Theory. Comput.* **8**, 1902 (2012).
- [37] K. Ishizuka and N. Uyeda, *Acta Cryst.* **33**, 740 (1977).
- [38] O. O. Kurakevch and V. L. Solozhenko, *Acta. Cryst.* **63**, i80 (2007).
- [39] R. E. Hughes, C. H. Kennard, D. B. Sullenger, H. A. Weakliem, D. E. Sands and J. L. Hoard, *J. Am. Chem. Soc.* **85**, 361 (1963).
- [40] J. L. Hoard, D. B. Sullenger, C. H. L. Kennard and R. E. Hughes, *J. Solid State Chem.* **1**, 268 (1970).
- [41] M. J. McKelvy, A. R. Rae Smith, and L. Eyring, *J. Solid State Chem.* **44**, 374 (1982).
- [42] P. Favia, T. Stoto, M. Carrard, P. A. Stadelmann, and L. Zuppiroli, *Microsc. Microanaly. Microstruct.* **7**, 225 (1996).